Amplitude analysis of the $D^+ \to \pi^-\pi^+\pi^+$ decay and measurement of the $\pi^-\pi^+$ S-wave amplitude

LHCb collaboration

Abstract

An amplitude analysis of the $D^+ \to \pi^-\pi^+\pi^+$ decay is performed with a sample corresponding to $1.5\,\text{fb}^{-1}$ of integrated luminosity of pp collisions at a centre-of-mass energy $\sqrt{s} = 8\,\text{TeV}$ collected by the LHCb detector in 2012. The sample contains approximately six hundred thousand candidates with a signal purity of 95%. The resonant structure is studied through a fit to the Dalitz plot where the $\pi^-\pi^+$ S-wave amplitude is extracted as a function of $\pi^-\pi^+$ mass, and spin-1 and spin-2 resonances are included coherently through an isobar model. The S-wave component is found to be dominant, followed by the $\rho(770)^0\pi^+$ and $f_2(1270)\pi^+$ components. A small contribution from the $\omega(782) \to \pi^-\pi^+$ decay is seen for the first time in the $D^+ \to \pi^-\pi^+\pi^+$ decay.

1 Introduction

Multi-body hadronic decays of charm particles offer an interesting environment for addressing a variety of phenomena related to the interplay of weak and strong interactions. Typically, the formation of three- and four-body final states proceeds through resonances as intermediate states, with rich interference patterns which allow the study of light meson spectroscopy, among other effects. This is particularly relevant for the controversial scalar sector, which poses a long-standing puzzle. With more states appearing below 2 GeV [1] than a naïve quark-antiquark nonet can accommodate,[1] there is an ongoing debate on their spectra and nature [2–6].

In three-body D decays, the $K\overline{K}$, $K\pi$ or $\pi\pi$ scattering amplitudes in the S-wave can be studied in the range from the corresponding threshold up to $\sim$1.5–1.8 GeV, thus providing information on meson-meson interactions that are complementary to those from scattering experiments. For the latter, the primary source of information on $L = 0$, $I = 0$ $\pi\pi$ amplitudes, in particular, comes from the reactions $\pi N \rightarrow \pi\pi N$, for $\pi\pi$ invariant mass above 0.6 GeV [7–11], and $K^+ \rightarrow \pi^-\pi^+ e^+\nu_e$ decays [12, 13], below 0.4 GeV. During the last two decades, the increasingly large D-decay data sets available from charm- and B-factories have provided new inputs to this field. Currently, the LHCb experiment has the largest samples of charm decays.

Decays of D mesons proceed through the weak decay of the charm quark together with the hadronisation forming the final-state mesons, including rescattering processes, before reaching the detector. Scattering amplitudes are, therefore, embedded in the total D-decay amplitude, and cannot be directly accessed. However, given that in general most of the decay rates of D mesons are accounted for by resonances, it is often assumed that the dynamics of the final states can be well represented as a quasi-two-body process ("2+1" approximation [14]) and are driven by meson-meson interactions. Nevertheless, effects of coupled channels, three-body interactions and the isospin degree of freedom may also play a role. At present, there are no tools for a complete description of such decay amplitudes from first principles. In this context, the study of the S-wave in different decay modes – many with broad and overlapping states for which the "2+1" approach is limited – may provide valuable inputs for phenomenological analyses.

The $D^+ \rightarrow \pi^-\pi^+\pi^+$ decay[2] is a valuable channel for studies of $\pi^-\pi^+$ interactions. Previous analyses of this decay [15–17] have shown a dominance of the S-wave component, with a $\sim 50\%$ contribution from the $f_0(500)$ meson. The dominant decay mechanism is expected to be the tree-level external W-radiation amplitude, illustrated in Fig. 1, thus the $\pi^-\pi^+$ amplitudes, including the S-wave one, are produced primarily from a $d\bar{d}$ source.

As a comparison, in the $D_s^+ \rightarrow \pi^-\pi^+\pi^+$ decay the S-wave contribution (produced via $s\bar{s}$) is also found to be dominant [18–20], but its main component is the $f_0(980)$ state, with no evidence for $f_0(500)$ production.

In this paper, the Dalitz plot of the $D^+ \rightarrow \pi^-\pi^+\pi^+$ decay is analysed, based on 1.5 fb^{-1} of pp collision data at 8 TeV centre-of-mass energy, collected by the LHCb experiment in 2012. The main purpose of this work is to determine the resonant structure of the decay and to study the $\pi^-\pi^+$ S-wave using a *quasi-model-independent* partial wave analysis (QMIPWA): no model is assumed for the S-wave amplitude, which is parameterised as a generic complex function to be determined by a fit to the data, while spin-1 and spin-2

---

[1]Natural units with $\hbar = c = 1$ are used.
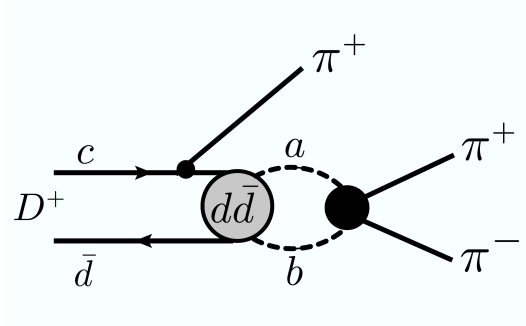[2]Charge conjugation is implicit throughout this paper.

Figure 1: Leading diagram for the $D^+ \to \pi^-\pi^+\pi^+$ decay. Possible rescattering effects are represented by the a, b meson pair.

states are included through an isobar model.

2 LHCb detector and simulation

The LHCb detector [21,22] is a single-arm forward spectrometer covering the pseudorapidity range $2 < \eta < 5$, designed for the study of particles containing b or c quarks. The detector includes a high-precision tracking system consisting of a silicon-strip vertex (VELO) detector surrounding the pp interaction region, a large-area silicon-strip detector located upstream of a dipole magnet with a bending power of about 4 Tm, and three stations of silicon-strip detectors and straw drift tubes placed downstream of the magnet. The tracking system provides a measurement of the momentum, p, of charged particles with a relative uncertainty that varies from 0.5% at low momentum to 1.0% at 200 GeV. The minimum distance of a track to a primary pp collision vertex (PV), the impact parameter (IP), is measured with a resolution of $(15 + 29/p_T) \, \mu\text{m}$, where p_T is the component of the momentum transverse to the beam, in GeV. Different types of charged hadrons are distinguished using information from two ring-imaging Cherenkov detectors. Photons, electrons and hadrons are identified by a calorimeter system consisting of scintillating-pad and preshower detectors, an electromagnetic and a hadronic calorimeter. Muons are identified by a system composed of alternating layers of iron and multiwire proportional chambers.

The online event selection is performed by a trigger system [23], which consists of a hardware stage, based on information from the calorimeter and muon systems, followed by a software stage, which applies a full event reconstruction. At the hardware-trigger stage, events are required to have a muon with high p_T or a hadron, photon or electron with high transverse energy in the calorimeters. The software trigger is divided into two parts. The first part employs a partial reconstruction of the tracks, and a requirement on p_T and IP is applied to, at least, one of the final-state particle forming the D^+ candidate. In the second part a full event reconstruction is performed and dedicated algorithms are used to select D^+ candidates decaying into three charged hadrons.

Simulation is used to model the effects of the detector acceptance and the selection requirements, to validate the fit models and to evaluate efficiencies. In the simulation, pp collisions are generated using PYTHIA [24] with a specific LHCb configuration [25].

Decays of unstable particles are described by EVTGEN [26], in which final-state radiation is generated using PHOTOS [27]. The interaction of the generated particles with the detector, and its response, are implemented using the GEANT4 toolkit [28] as described in Ref. [29]. For part of the total simulation sample, the underlying pp interaction is reused multiple times, with an independently generated signal decay for each [30].

3 $D^+ \to \pi^- \pi^+ \pi^+$ selection

In the offline selection, combinations of three charged particles with net charge ± 1 must form a good-quality vertex well detached from any PV. The PV associated to the D^+ candidate is chosen as that with the smallest value of χ^2_{IP}, where χ^2_{IP} is defined as the difference in the vertex-fit χ^2 of the PV reconstructed with and without the particle under consideration, in this case the D^+ candidate. Requirements are placed on the following variables: the significance of the distance between the PV and the D^+ decay vertex; the angle between the reconstructed D^+ momentum vector and the vector connecting the PV to the decay vertex; the χ^2 of the D^+ decay vertex fit; the distance of closest approach between any two final-state tracks; the momentum, the transverse momentum and the χ^2_{IP} of the D^+ candidate and of its decay products. The invariant mass of the D^+ candidates, calculated using the pion mass hypothesis for the three tracks, is required to be within the interval [1800,1940] MeV.

Particle identification (PID) is also used to separate pions from kaons and muons. The requirements, placed on all tracks, reduce to the percent level the cross-feed from decays such as $D^0 \to K^- \pi^+$ plus an unrelated track, $D^+ \to K^- \pi^+ \pi^+$ and $D^+ \to \mu^- \pi^+ \pi^+ \overline{\nu}_\mu$. The $D^+ \to K^0_S \pi^+$ decay is removed by vetoing candidates with $\pi^+ \pi^-$ invariant mass in the interval [0.485,0.500] GeV.

A multivariate analysis (MVA) [31] is used to further reduce the remaining backgrounds, mostly from random association of three charged tracks, but also from contamination of $D^+_{(s)} \to (\eta^{(\prime)} \to \pi^+ \pi^- \gamma) \pi^+$ decays, where the photon is not detected. The MVA uses a Gradient Boosted Decision Tree (BDTG) [32] as a classifier and is based on the same quantities (or combinations of them) used in the online selection, but avoiding those that can potentially cause large efficiency variation across the Dalitz plot, such as the χ^2_{IP} and p_{T} of the decay products. For training, simulated $D^+ \to \pi^- \pi^+ \pi^+$ decays are used to represent the signal, whereas data from the invariant-mass sidebands ([1810,1830] and [1910,1930] MeV) of the signal peak are used for the background. Before performing the MVA, a weighting procedure [33] is used to account for small differences between the simulation and data, including differences in the momentum and transverse momentum distributions of the decay products. The data are divided into two independent sets in a pseudorandom manner. The $\pi^- \pi^+ \pi^+$ mass spectrum of one of the datasets is fitted using the sPlot technique [34] to obtain signal and background weights needed to determine the distributions of the quantities to be used in the MVA, as well as the kinematic distributions, needed for a weighting procedure explained above. The second dataset, corresponding to an integrated luminosity of about $0.75 \, \text{fb}^{-1}$, is used to select the final candidates for the Dalitz plot analysis.

The requirement on the BDTG output is chosen to yield a sample of $D^+ \to \pi^- \pi^+ \pi^+$ decays with 95% purity in order to reduce the impact of systematic effects related to the background modelling in the Dalitz plot fit. The efficiency drops very rapidly for more

stringent requirements, with only a modest gain in purity.

The invariant mass of $D^+ \to \pi^-\pi^+\pi^+$ candidates after all requirements is shown in Fig. 2. An extended binned maximum-likelihood fit to this distribution is performed. The probability distribution function (PDF) of the signal is represented by a sum of a Gaussian function and two Crystal Ball (CB) [35] functions, while the background is modelled by an exponential function. The signal PDF is

$$P_{\text{sig}}[m(\pi^-\pi^+\pi^+)] = f_{\text{G}} \times \text{G}(\mu, \sigma_{\text{G}}) + (1 - f_{\text{G}}) \times [f_{\text{CB}} \times \text{CB}_1(\mu, R_1\sigma_{\text{G}}, \alpha_1, N_1) +$$
$$(1 - f_{\text{CB}}) \times \text{CB}_2(\mu, R_2\sigma_{\text{G}}, \alpha_2, N_2)], \quad (1)$$

where μ and σ_{G} are the mean value and the width of the Gaussian function G. The two Crystal Ball functions, CB_1 and CB_2, have widths $R_1\sigma_{\text{G}}$ and $R_2\sigma_{\text{G}}$, and tail parameters α_1, N_1 and α_2, N_2. A common parameter, μ, describes the most probable mass value of the two Crystal Balls and the mean of the Gaussian function. The fractions of each PDF component are f_{G} for the Gaussian function, $(1-f_{\text{G}}) \times f_{\text{CB}}$ for CB_1 and $(1-f_{\text{G}}) \times (1-f_{\text{CB}})$ for CB_2. The parameters α_i, N_i, R_i, f_{CB} and f_{G} defining the signal PDF are fixed to the values obtained from a fit to the simulated sample, while the parameters μ and σ_G are allowed to float freely.

For the Dalitz Plot analysis, candidates are selected within a $2\sigma_{\text{eff}}$ mass window around the mean μ, where the effective mass resolution, σ_{eff}, is defined by $\sigma_{\text{eff}} = \sqrt{[f_{\text{G}} + (1-f_{\text{G}})f_{\text{CB}}R_1^2 + (1-f_{\text{G}})(1-f_{\text{CB}})R_2^2]\,\sigma_{\text{G}}^2} = 8.7\,\text{MeV}$. The final sample has $601\,171$ candidates with a signal purity of $(95.2 \pm 0.1)\%$ in the corresponding mass interval of $[1854.1, 1889.0]\,\text{MeV}$. Multiple candidates in the same event correspond to only 0.15% of the final sample and are retained.

The Dalitz plot distribution of the selected candidates is shown in Fig. 3. The axes are the Dalitz variables $s_{12} \equiv (p_1 + p_2)^2$ and $s_{13} \equiv (p_1 + p_3)^2$, where p_i $(i = 1, 2, 3)$ are the 4-momenta of the three pions in the final state and the particle ordering is such that the pion with charge opposite to that of the D^+ meson is always particle 1, and the same-sign pions are randomly assigned particles 2 and 3. These Lorentz-invariant quantities are computed after refitting tracks with the constraint on the invariant mass of the candidate to the known D^+ mass [1].

4 Background and efficiency models

The remaining background in the $D^+ \to \pi^-\pi^+\pi^+$ sample, which amounts to 4.8%, needs to be parameterised to be included in the Dalitz plot fit. The background distribution is inferred from the sidebands of the $D^+ \to \pi^-\pi^+\pi^+$ invariant-mass signal region, specifically, the intervals $[1810, 1830]\,\text{MeV}$ and $[1910, 1930]\,\text{MeV}$. The background within the signal region is assumed to be the average composition of both sidebands. The candidates in these regions are projected to the Dalitz plot and a two-dimensional (2D) cubic spline procedure [36] is used to smooth the distribution in order to avoid binning discontinuities. The resulting model, shown in Fig. 4 (left), is used in the Dalitz plot fit.

The signal distribution in the Dalitz plot includes efficiency effects, which need to be corrected for. The efficiency model across the Dalitz plot includes the effects of the geometrical acceptance of the detector, as well as reconstruction, trigger, selection, and PID requirements. All these effects apart from those associated with PID are quantified using simulation. The PID efficiencies for the pions are evaluated from calibration
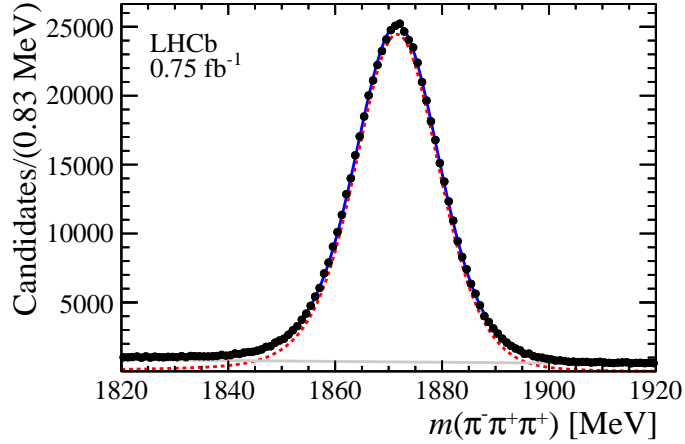
Figure 2: Invariant-mass distribution of $D^+ \to \pi^-\pi^+\pi^+$ candidates after final selection, with the fit result superimposed (blue solid line). The dashed red line and the solid gray line correspond to the signal and background components of the fit, respectively.
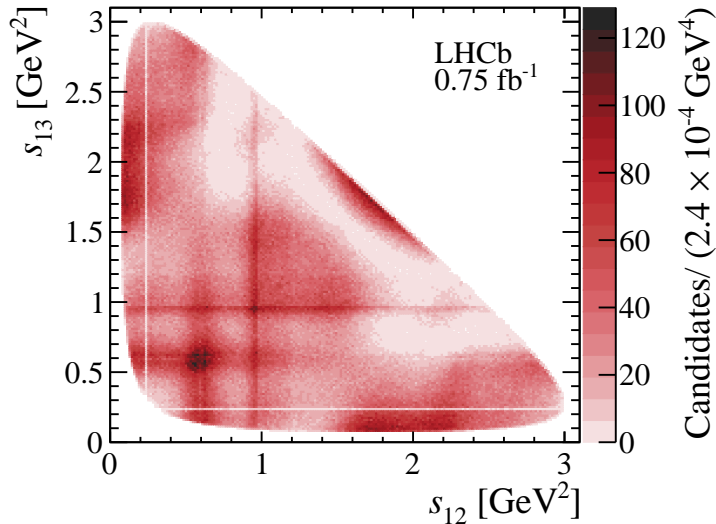

Figure 3: Dalitz plot distribution of the final $D^+ \to \pi^-\pi^+\pi^+$ sample. The lines in the interval $[0.235, 0.250]\,\text{GeV}^2$ correspond to the veto applied to remove $D^+ \to K_S^0\pi^+$ decays.

samples of $D^{*+} \to D^0(\to K^-\pi^+)\pi^+$ decays [37] and depend on the particle momentum, pseudorapidity and charged-particle multiplicity. The final efficiency model is constructed from a two-dimensional histogram with 15×15 uniform bins which is then smoothed by a 2D cubic spline, as shown in Fig. 4 (right).

5 The QMIPWA formalism

The Dalitz plot of $D^+ \to \pi^-\pi^+\pi^+$ candidates shown in Fig. 3 shows a rich resonant structure: contributions from the subchannels $\rho(770)^0\pi^+$ (with an evident interference with $\omega(782)\pi^+$), $f_0(500)\pi^+$, $f_0(980)\pi^+$ and possible high-mass vector and tensor states
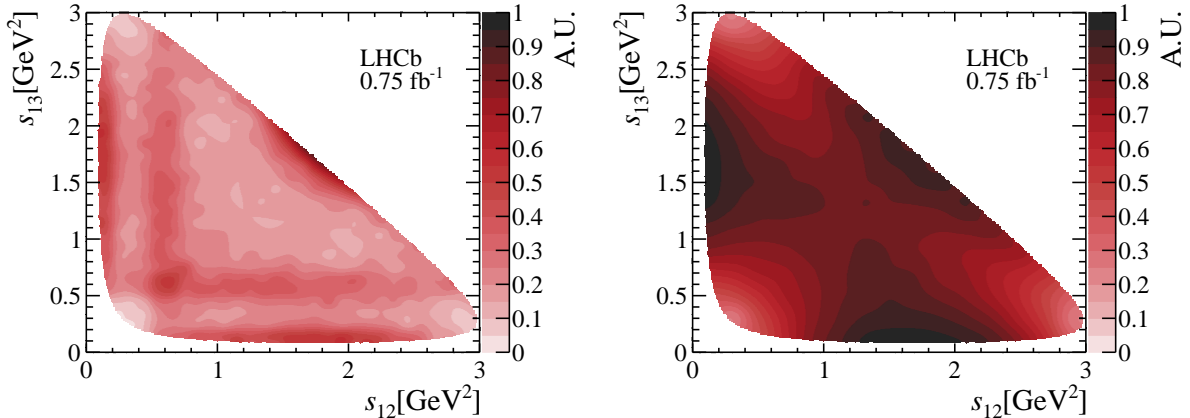
Figure 4: Models for (left) background distribution and (right) signal efficiency across the Dalitz plot, where the z-axis scale is arbitrary.

are seen. To disentangle these contributions, a full amplitude analysis is needed. The approach of this work is to describe the total $D^+ \to \pi^-\pi^+\pi^+$ amplitude as a coherent sum of an S-wave contribution and higher-spin waves,

$$\mathcal{A}(s_{12}, s_{13}) = \left[\mathcal{A}_{\text{S-wave}}(s_{12}) + \sum_i a_i e^{i\delta_i} \mathcal{A}_i(s_{12}, s_{13}) \right] + (s_{12} \leftrightarrow s_{13}), \qquad (2)$$

where the total amplitude is Bose-symmetrised with respect to s_{12} and s_{13} due to the two identical pions. The first term is the S-wave amplitude,

$$\mathcal{A}_{\text{S-wave}}(s_{12}) = a_0(s_{12}) e^{i\delta_0(s_{12})}, \qquad (3)$$

where the real functions $a_0(s_{12})$ and $\delta_0(s_{12})$ are to be determined by the Dalitz plot fit: the $\pi^-\pi^+$ invariant-mass spectrum is divided in 50 intervals (knots) where interpolation to obtain a continuous S-wave complex function is attained through a linear spline. The P- and D-wave components are included through an isobar model, represented by the terms in the sum in Eq. 2, where $\mathcal{A}_i(s_{12}, s_{13})$ is the complex amplitude of resonance R_i, with magnitude a_i and phase δ_i as free parameters. This approach to the total amplitude is referred to as *quasi-model-independent* since any limitation of the isobar model to describe the higher-spin components may reflect in the description of the S-wave amplitude which has 100 free parameters.

Within the isobar model, the individual resonant amplitude for a process of type $D \to R_i c; R_i \to a b$, where R_i is an intermediate resonant state, is written as

$$\mathcal{A}_i(s_{ab}, s_{ac}) = F_D^J F_R^J \mathcal{M}_J T_{R_i}(s_{ab}). \qquad (4)$$

Since the D^+ meson and the final-state pions are spinless particles, the spin of the resonance, J, is equal to the orbital angular momentum in both the decays $D \to R_i c$ and $R_i \to a b$.

The Blatt-Weisskopf barrier factors [38], F_D^J and F_R^J, take into account the finite size of the D meson and the R_i resonance in the decay processes $D \to R_i c$ and $R_i \to a b$, respectively. They are functions of $z = rp^*$, as shown in Table 1, where r is the effective

Table 1: Spin-dependent Blatt-Weisskopf barrier factors.

Spin	Blatt-Weisskopf factor
$J = 1$	$\sqrt{\dfrac{1 + z_0^2}{1 + z^2}}$
$J = 2$	$\sqrt{\dfrac{z_0^4 + 3z_0^2 + 9}{z^4 + 3z^2 + 9}}$

radius of the decaying particle, p^* is the modulus of the momentum of the decay products measured in the decaying particle rest frame, and z_0 is the value of z calculated at the known mass of the decaying particle. In this analysis, the effective radii of the D^+ meson and the intermediate resonances are set to 5 GeV^{-1} and 1.5 GeV^{-1}, respectively [15,39–41].

The function $\mathcal{M}_J$ describes the angular distribution of the decay particles in the Zemach formalism [42] with explicit forms for $J = 1$ and $J = 2$ given by

$$\mathcal{M}_1 = s_{bc} - s_{ab} + \left(\frac{1}{s_{ab}}(m_D^2 - m_c^2)(m_a^2 - m_b^2) \right), \tag{5}$$

and

$$\mathcal{M}_2 = \mathcal{M}_1^2 - \frac{1}{3} \left(s_{ab} - 2m_D^2 - m_c^2 + \frac{1}{s_{ab}}(m_D^2 - m_b^2)^2 \right) \times$$
$$\left(s_{ab} - 2m_a^2 - 2m_c^2 + \frac{1}{s_{ab}}(m_a^2 - m_b^2)^2 \right), \tag{6}$$

respectively, where m_D is the known mass of the D meson and m_a, m_b and m_c those of the decay products. It is clear that these expressions take a simpler form for the particular case when there are three charged pions in the final state ($m_a = m_b = m_c = m_\pi$).

The dynamical function $T_{R_i}(s_{ab})$ in Eq. 4 represents the resonance lineshape, usually a relativistic Breit-Wigner (RBW),

$$T_{\mathrm{RBW}}(s_{ab}) = \frac{1}{m_0^2 - s_{ab} - im_0\Gamma(s_{ab})}, \tag{7}$$

where m_0 is the nominal mass of the resonance and $\Gamma(s_{ab})$ is the mass-dependent width which is given by

$$\Gamma(s_{ab}) = \Gamma_0 \frac{m_0}{\sqrt{s_{ab}}} \left(\frac{p^*}{p_0^*} \right)^{2J+1} (F_R^J)^2, \tag{8}$$

with Γ_0 being the nominal width of the resonance.

A Gounaris-Sakurai (GS) function [43] is a modification of the RBW lineshape, commonly used to describe the pion electromagnetic form factor in the parameterisation of spin-1 ρ-type resonances,

$$T_{\mathrm{GS}}(s_{ab}) = \frac{1 + \Gamma_0 d/m_0}{(m_0^2 - s_{ab}) + f(s_{ab}) - im_0\Gamma(s_{ab})}, \tag{9}$$

where

$$f(s_{ab}) = \Gamma_0 \frac{m_0^2}{p_0^{*3}} \left\{ p^{*2} \left[h(s_{ab}) - h(m_0^2) \right] + \left(m_0^2 - s_{ab} \right) p_0^{*2} \left. \frac{\mathrm{d}h}{\mathrm{d}s_{ab}} \right|_{m_0^2} \right\} . \tag{10}$$

The function $h(s_{ab})$ is given by

$$h(s_{ab}) = \frac{2}{\pi} \frac{p^*}{\sqrt{s_{ab}}} \ln \left(\frac{\sqrt{s_{ab}} + 2p^*}{2m_\pi} \right) , \tag{11}$$

where m_π is the pion mass and the derivative is given by

$$\left. \frac{\mathrm{d}h}{\mathrm{d}s_{ab}} \right|_{m_0^2} = h(m_0^2) \left[(8p_0^{*2})^{-1} - (2m_0^2)^{-1} \right] + (2\pi m_0^2)^{-1} . \tag{12}$$

The parameter $d = f(0)/(\Gamma_0 m_0)$ is given by

$$d = \frac{3}{\pi} \frac{m_\pi^2}{p_0^{*2}} \ln \left(\frac{m_0 + 2p_0^*}{2m_\pi} \right) + \frac{m_0}{2\pi\, p_0^*} - \frac{m_\pi^2 m_0}{\pi\, p_0^{*3}} . \tag{13}$$

In this analysis, the GS lineshape is used for the spin-1 ρ-type resonances, while the RBW lineshape is used for other resonances such as the $\omega(782)$ and $f_2(1270)$ states. The values m_0 and Γ_0 for all resonances are fixed in the fit to their known values [1].

The $\omega(782) \to \pi^-\pi^+$ decay violates isospin, and it is not clear whether this process occurs through direct decay or through mixing with the $\rho(770)^0$ state (or both). As an alternative to representing the $\rho(770)\pi^+$ and $\omega(782)\pi^+$ amplitudes as a sum of isobars, their combined contribution is parametrised through a $\rho-\omega$ mixing lineshape given by [44]

$$T_{\rho-\omega} = T_\rho \left[\frac{1 + \Delta|B|e^{i\phi_B}T_\omega}{1 - \Delta^2 T_\rho T_\omega} \right] , \tag{14}$$

where T_ρ and T_ω are the GS and RBW lineshapes for the $\rho(770)^0$ and $\omega(782)$ resonances, respectively. The magnitude $|B|$ and the phase ϕ_B quantify the relative contribution of the $\omega(782)$ and the $\rho(770)$ resonances, and are free parameters in the fit. The factor $\Delta = \delta(m_0^\rho + m_0^\omega)$ governs the electromagnetic mixing of these states, where the value of δ is fixed to $2.15\,\mathrm{MeV}$ [44] and m_0^ρ and m_0^ω are the known masses [1]. This parameterisation is equivalent to that used in Ref. [45] given that Δ^2 is small and therefore the term where it appears in the denominator can be neglected.

6 The Dalitz plot fit methodology

Given the large data sample, the large number of parameters used in the decay amplitude, and the need to normalise the total PDF at each iteration of the minimisation process, the GooFit framework [46] for maximum-likelihood fits is used. GooFit is based on GPU acceleration with parallel processing.

An unbinned maximum-likelihood fit to the data distribution in the Dalitz plot is performed. The likelihood function is written as a combination of the signal and background PDFs given by

$$\mathcal{L} = \prod_i \left\{ f_{\mathrm{sig}} \times \mathcal{P}_{\mathrm{sig}}^i \left(s_{12}, s_{13} \right) + (1 - f_{\mathrm{sig}}) \times \mathcal{P}_{\mathrm{bkg}}^i \left(s_{12}, s_{13} \right) \right\} , \tag{15}$$

where f_{sig} is the signal fraction and the product runs over the candidates in the final data sample. The background PDF, $\mathcal{P}_{\text{bkg}}(s_{12}, s_{13})$, is the normalised background model, and is provided as the high definition histogram shown in Fig. 4. The normalised signal PDF, $\mathcal{P}_{\text{sig}}(s_{12}, s_{13})$, is given by

$$\mathcal{P}_{\text{sig}}(s_{12}, s_{13}) = \frac{\epsilon(s_{12}, s_{13}) \left| \mathcal{A}(s_{12}, s_{13}) \right|^2}{\iint_{\text{DP}} \epsilon(s_{12}, s_{13}) \left| \mathcal{A}(s_{12}, s_{13}) \right|^2 ds_{12} ds_{13}}, \tag{16}$$

where $\epsilon(s_{12}, s_{13})$ is the efficiency model function included as the smoothed histogram shown in Figure 4; the denominator is the integral of the numerator over the Dalitz plot (DP) to guarantee that $\mathcal{P}_{\text{sig}}(s_{12}, s_{13})$ is normalised at each iteration of the minimisation process. The fit parameters are the 50 pairs of magnitudes and phases of the S-wave amplitude, and the magnitudes and phases of the higher-spin components, except the $\rho(770)^0 \pi^+$ channel which is taken as the reference mode, with magnitude fixed to 1 and phase fixed to zero. The set of optimal parameters is determined by minimising the quantity $-2 \log \mathcal{L}$ using the MINUIT [47] package.

The fit fraction for the ith intermediate channel is defined as

$$\text{FF}_i = \frac{\iint_{\text{DP}} \left| a_i e^{i\delta_i} \mathcal{A}_i(s_{12}, s_{13}) \right|^2 ds_{12} ds_{13}}{\iint_{\text{DP}} \left| \sum_j a_j e^{i\delta_j} \mathcal{A}_j(s_{12}, s_{13}) \right|^2 ds_{12} ds_{13}}. \tag{17}$$

Due to interference, the sum of fit fractions can be less than or greater than 100%. Interference fit fractions can also be defined, quantifying the level of interference between any pair i, j $(i \neq j)$ of amplitude components,

$$\text{FF}_{ij} = \frac{\iint_{DP} 2 \, \text{Re} \left[a_i a_j e^{i(\delta_i - \delta_j)} \mathcal{A}_i(s_{12}, s_{13}) \mathcal{A}_j^*(s_{12}, s_{13}) \right] ds_{12} ds_{13}}{\iint_{\text{DP}} \left| \sum_k a_k e^{i\delta_k} \mathcal{A}_k(s_{12}, s_{13}) \right|^2 ds_{12} ds_{13}}. \tag{18}$$

By construction, the sum of fit fractions and interference terms is 100%.

The fit quality is measured through the statistical quantity χ^2 defined as

$$\chi^2 = \sum_{i=1}^{N_b} \chi_i^2 = \sum_{i=1}^{N_b} \frac{(N_i^{\text{obs}} - N_i^{\text{est}})^2}{\sigma_i^2}, \tag{19}$$

where the Dalitz plot is divided in N_b bins and, for each bin, the number of observed candidates, N_i^{obs}, the number of candidates estimated from the fit model, N_i^{est}, and the uncertainty on their difference, σ_i, are obtained. For unbinned maximum-likelihood fits, the number of degrees of freedom (ndof) range as $[N_b - q - 1, N_b - 1]$ [48], where q is the number of free parameters, and it is used to calculate the corresponding range of χ^2/ndof. This is done using the *folded* Dalitz plot – due to the symmetry of the $D^+ \to \pi^- \pi^+ \pi^+$ Dalitz plot with respect to the axis $s_{13} = s_{12}$, the variables s_{high} and s_{low} are defined, respectively, as the higher and the lower values of each pair (s_{12}, s_{13}). The folded Dalitz plot is divided in $N_b = 625$ bins using an adaptive binning algorithm, such that all bins have the same population. Besides the χ^2/ndof, the value of $-2 \log \mathcal{L}$ is also used to compare models. In addition, the distribution of residuals $(N_i^{\text{obs}} - N_i^{\text{est}})/\sigma_i$ across the folded Dalitz plot is used for visual inspection of any local discrepancy between fit model and data, which are also compared through the projections of s_{high}, s_{low}, the sum of these projections, denoted $s_{\pi^- \pi^+}$, and $s_{23} \equiv (p_2 + p_3)^2$.

9

7 Dalitz plot fit results

The $D^+ \to \pi^-\pi^+\pi^+$ amplitude fit model is constructed with the scalar sector represented through the QMIPWA approach using 50 knots, and starting with the spin-1 and spin-2 states observed from previous analyses of this decay (E791 [15], FOCUS [16] and CLEO [17] collaborations, with much smaller datasets): $\rho(770)^0\pi^+$, $\rho(1450)^0\pi^+$ and $f_2(1270)\pi^+$, plus the $\omega(782)\pi^+$ channel, not observed in previous analyses but clearly seen in Fig. 3. From that, other possible states, such as $f_2'(1525)$, $\rho(1700)^0$, $\rho_3(1690)$,[3] are added one at a time until a good representation of the data is found.

The best model is achieved when the $\rho(1700)^0$ resonance is added; attempts to include further states do not bring significant improvements. This model has 108 free parameters. Table 2 summarises the results from the fit, including systematic uncertainties discussed later in Sec.8. Interference fit fractions are shown in Table 3. The projections and the distribution of residuals are shown in Fig. 5, showing overall a good agreement between the data and fit model.

Table 2: Dalitz fit results for magnitudes, phases and fit fractions (%) of the spin-1 and spin-2 components, and the S-wave fit fraction. The uncertainties quoted are, in order, statistical, experimental systematics, and model systematics.

Component	Magnitude	Phase [°]	Fit fraction [%]
$\rho(770)^0\pi^+$	1 [fixed]	0 [fixed]	$26.0 \pm 0.3 \pm 1.6 \pm 0.3$
$\omega(782)\pi^+$	$(1.68 \pm 0.06 \pm 0.15 \pm 0.02) \times 10^{-2}$	$-103.3 \pm 2.1 \pm 2.6 \pm 0.4$	$0.103 \pm 0.008 \pm 0.014 \pm 0.002$
$\rho(1450)^0\pi^+$	$2.66 \pm 0.07 \pm 0.24 \pm 0.22$	$47.0 \pm 1.5 \pm 5.5 \pm 4.1$	$5.4 \pm 0.4 \pm 1.3 \pm 0.8$
$\rho(1700)^0\pi^+$	$7.41 \pm 0.18 \pm 0.47 \pm 0.71$	$-65.7 \pm 1.5 \pm 3.8 \pm 4.6$	$5.7 \pm 0.5 \pm 1.0 \pm 1.0$
$f_2(1270)\pi^+$	$2.16 \pm 0.02 \pm 0.10 \pm 0.02$	$-100.9 \pm 0.7 \pm 2.0 \pm 0.4$	$13.8 \pm 0.2 \pm 0.4 \pm 0.2$
S-wave			$61.8 \pm 0.5 \pm 0.6 \pm 0.5$
$\sum_i \mathrm{FF}_i$			112.8
χ^2/ndof (range)	[1.47 - 1.78]		$-2\log\mathcal{L} = 805622$

Table 3: Dalitz fit results for the interference fit fractions (%) (statistical uncertainties only).

	$\omega(782)\pi^+$	$\rho(1450)^0\pi^+$	$\rho(1700)^0\pi^+$	$f_2(1270)\pi^+$	S-wave
$\rho(770)^0\pi^+$	-0.24 ± 0.06	5.1 ± 0.3	-5.8 ± 0.4	-0.3 ± 0.1	1.8 ± 0.4
$\omega(782)\pi^+$		0.05 ± 0.01	0.05 ± 0.01	0.046 ± 0.04	-0.04 ± 0.01
$\rho(1450)^0\pi^+$			-4.0 ± 0.5	1.1 ± 0.1	1.7 ± 0.2
$\rho(1700)^0\pi^+$				-0.8 ± 0.1	-3.4 ± 0.5
$f_2(1270)\pi^+$					-1.6 ± 0.1

The S-wave component is found to be the dominant contribution, with a fraction of almost 62%, in agreement with previous observations based on the isobar model. The $\rho(770)^0\pi^+$ channel is the second greatest contribution ($\sim 26\%$), followed by the $f_2(1270)\pi^+$ mode ($\sim 14\%$). The two heavy ρ states contribute at the 5% level, with a destructive interference pattern evidenced by an interference fit fraction of the same order.

As anticipated by visual inspection, there is a small but clear contribution from the resonant state $\omega(782)$, with an interference pattern with $\rho(770)^0$, which can also be seen in the $s_{\pi^-\pi^+}$ projection in Fig. 5. This contribution was not observed in previous analyses

---

[3]Since the $\rho_3(1690)$ state was not found to be significant, the formalism for spin-3 resonances is not described in Sec. 5.
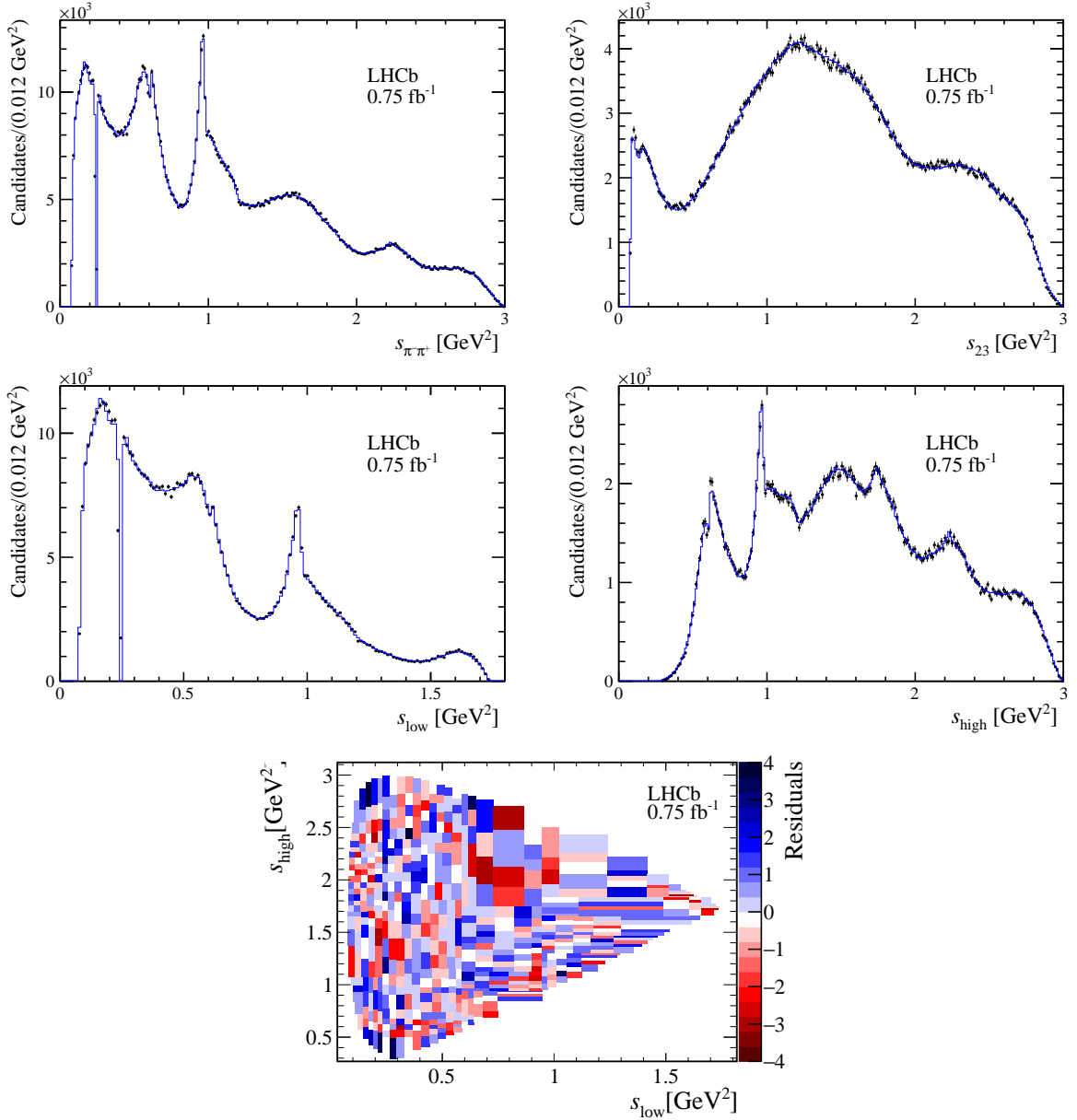
Figure 5: Dalitz plot projections of (top left) $s_{\pi^-\pi^+}$, (top right) s_{23}, (middle left) s_{low}, and (middle right) s_{high} projections, where the (red) points are data and the (blue) line is the fit model result, with the fit normalised residuals displayed in the bottom plot.

due to their limited datasets, thus this effect is observed for the first time in this analysis. The alternative parameterisation of the $\rho - \omega$ mixing lineshape shown in Eq. 14 was tested, with $|B|$ and ϕ_B as free parameters. The outcome of the fit represents essentially the same solution: a difference in $-2\log\mathcal{L}$ of only $+1$ unit, no significant differences in all the other fit parameters, and the resulting $\rho - \omega$ amplitude being almost indistinguishable to that of the sum of $\rho(770)^0$ and $\omega(782)$ isobars. The values found for $\rho - \omega$ mixing parameters are $|B| = 0.52 \pm 0.02 \pm 0.05 \pm 0.01$ and $\phi_B = (158.8 \pm 2.1 \pm 2.6 \pm 0.4)°$, where the quoted uncertainties are, in order, statistical, experimental systematics and model systematic uncertainties.
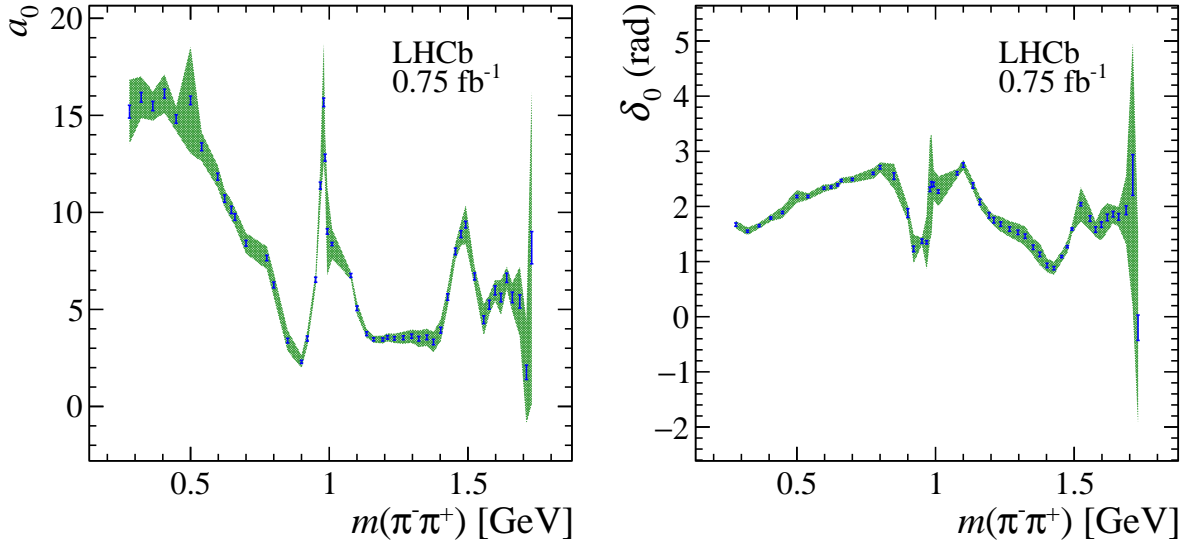
Figure 6: Fitted (left) magnitude and (right) phase of the $\pi^-\pi^+$ S-wave amplitude with statistical uncertainties as the blue bars and the total uncertainties (combined statistical, experimental and model systematics) as the green bands.

While the contribution of the $\rho(1450)^0$ resonance has been reported previously in the $D^+ \to \pi^-\pi^+\pi^+$ decay [15], this state alone is not enough to describe the $\pi^-\pi^+$ P-wave amplitude at high mass. The inclusion of the $\rho(1700)^0$ resonance in the model improves the fit significantly, resulting in a difference in $-2\log\mathcal{L}$ of -488 units compared to that of the model without it. Its contribution is robust, with its stability in the fit being tested through many fit variations (as part of the systematic studies discussed in Sec. 8). The $\rho(1700)^0$ is a broad state (nominal width of $250 \pm 100\,\text{MeV}$ [1]), and its inclusion affects the whole Dalitz plot, with an interesting interference pattern with the other vector states, in particular with the $\rho(1450)^0$ resonance. The results presented here provide input for the debate of $\rho(1450)^0 - \rho(1700)^0$ interference, supporting the need for these two overlapping states to exist (see for instance the entry for $\rho(1700)^0$ under "Particle listings" in [1]). Note that if these states are excitations of the $\rho^0(770)$, their production should be also favoured in the D^+ decay.

The S-wave amplitude obtained from the final-model fit is shown in Fig. 6. The values of the magnitude and phases for each knot are shown in Table 4. The magnitude $a_0(m_{\pi^-\pi^+})$ is large close to threshold and decreases until $\sim 0.9\,\text{GeV}$, with a steady phase increase, as expected from the dominant $f_0(500)$ contribution reported in previous analyses, and consistent with a $d\bar{d}$ source of the $D^+ \to \pi^-\pi^+\pi^+$ weak decay. Starting at $m(\pi^-\pi^+) \sim 0.9\,\text{GeV}$ the $f_0(980)$ signature is observed both as a sharp increase of the magnitude and a rapid variation (decrease and increase) in the phase, enhanced possibly by the opening of the $K\overline{K}$ channel. Starting at about $m(\pi^-\pi^+) \sim 1.4\,\text{GeV}$ and peaking near $m(\pi^-\pi^+) \sim 1.5\,\text{GeV}$, another structure in the amplitude with a corresponding phase movement is observed, indicating the presence of at least one more scalar resonance, possibly $f_0(1370)$ or $f_0(1500)$, or a combination of the two.

12

8 Systematic uncertainties

The systematic uncertainties on the fit parameters are divided into two categories: first those coming from the impact of experimental aspects; and second, referred to as model systematics, those corresponding to the uncertainties in resonance lineshape parameters such as masses, widths and form factors.

In the first category, effects due to the efficiency modelling, background contributions and intrinsic fit biases are considered. For the efficiency map, uncertainties arise from the finite size of the simulation samples, the effect of the binning scheme of the efficiency histogram prior to the 2D spline smoothing, and the procedure for obtaining PID efficiencies from the calibration samples. The first effect is estimated by generating a set of alternative efficiency histograms where the bin contents are varied according to a Poisson distribution, and performing the Dalitz fit with each alternative map. The root mean square (rms) of the distribution of each of the fit parameters is assigned as the corresponding systematic uncertainty. The systematic uncertainty due to the binning scheme of the efficiency map is assessed by performing the fits with smoothed efficiency maps obtained from varying the binning grid of the efficiency histogram from 15×15 (default) to 12×12 and 20×20. The largest variation in each fit parameter is assigned as the systematic uncertainty. The dominant uncertainties on the PID efficiency are due to the finite size of the calibration samples; the effect is assessed by varying the efficiencies from the calibration tables according to a Gaussian distribution centered at the nominal values and with widths equal to the statistical uncertainties, and obtaining new smoothed efficiency maps to refit the Dalitz plot and assess the impact on the fit parameters.

The effect of the signal-to-background ratio is estimated by varying the signal purity obtained from the invariant-mass fit within one standard deviation, repeating the Dalitz fit and assigning the difference in each parameter as the systematic uncertainty. The impact of the background model is addressed by determining it from either just the lower or just the higher mass sideband, and assigning the largest deviation in each fit parameter as the corresponding systematic uncertainty. The S-wave interval definition (knots in $m_{\pi^-\pi^+}$) is varied both in the number of knots (from 45 to 55) and position of the knots, the resulting S-wave amplitude in each case after the fit is used to calculate the values of magnitude and phase in the original knot scheme and the rms in each fit parameter (including those from spin-1 and spin-2 states) is assigned as systematic uncertainty.

Finally, uncertainties due to biases from the fitting algorithm, including the ability to reproduce a given (continuous) S-wave amplitude, are assessed by generating a large number of pseudoexperiments given by the full PDF (signal and background). The PDF for the signal model has its parameters set to those obtained from a QMIPWA fit with an alternative 50-knot choice using an adaptive binning where the division is made to equalise the event population. The pseudoexperiments are fitted with the baseline 50-knot model, and the rms of the distribution of the difference in each parameter is assigned as the systematic uncertainty. Overall, the largest systematic uncertainties come from the finite size of the simulation samples, the efficiency map binning, and the fit bias. The systematic uncertainties are all added in quadrature and comprise the second uncertainty in Tables 2 and 4. Other studies are performed as cross-checks and lead to variations within statistical uncertainties: the use of the efficiency map without correcting for mismatches between data and simulation; splitting the sample in terms of magnet orientation during data taking; and studying the effect of mass resolution around the region of the narrow $\omega(782)$

state.

In the second category, isobar model systematics, two studies are performed. First, the mass and the width of all the spin-1 and spin-2 states are varied within their quoted uncertainties [1], and the rms of the difference in each fit parameter is assigned as a systematic uncertainty. The second study addresses the impact of changing the effective radii of both the resonances and the D^+ meson used in the Blatt-Weisskopf barrier factors, to 1.0 and 2.0 GeV^{-1} and to 4.0 and 6.0 GeV^{-1}, respectively, and the largest variation for each parameter is assigned as systematic uncertainty. These two effects are added in quadrature and comprise the third uncertainties presented in Tables 2 and 4.

9 Summary and conclusions

This paper presents a Dalitz plot analysis of the $D^+ \to \pi^-\pi^+\pi^+$ decay. Using a sample containing more than six hundred thousand candidates, with a purity of 95%, the resonant structure of the decay is studied using the QMIPWA method, where the magnitude and the phase of the S-wave amplitude is obtained as a function of $m_{\pi^-\pi^+}$, while the spin-1 and spin-2 contributions are included with an isobar model. This approach is motivated by the presence of broad and overlapping light scalar resonances below 2 GeV, with poorly known masses and widths.

The result of the Dalitz plot fit shows that the decay is dominated by the $\pi^-\pi^+$ S-wave component corresponding to nearly 62% of the $D^+ \to \pi^-\pi^+\pi^+$ decay rate, which is consistent with results from previous analyses. The P-wave amplitude is the second largest component, led by the $\rho(770)^0$ contribution at the level of 26% but including also the $\omega(782)$ resonance and the high-mass states $\rho(1450)^0$ and $\rho(1700)^0$. The D-wave amplitude, consisting only of the $f_2(1270)$ state, accounts for about 14% of the $D^+ \to \pi^-\pi^+\pi^+$ decay rate.

The contribution of $D^+ \to \omega(782)\pi^+$ in the $D^+ \to \pi^-\pi^+\pi^+$ decay is observed for the first time, with a fit fraction of $(0.103 \pm 0.016)\%$. The $\omega(782) \to \pi^-\pi^+$ decay is isospin violating and has been observed in association with the $\rho(770) \to \pi^-\pi^+$ in a few processes with very different interference patterns [41, 45, 49–53].

Interesting structures are observed in the S-wave amplitude shown in Fig. 6. The broad structure near threshold is associated with the $f_0(500)$ resonance in model-dependent analyses, the $f_0(980)$ state is clearly visible with an asymmetric peak lineshape, and a further peak with corresponding phase variation is observed around 1.5 GeV indicating the presence of a further high-mass scalar state.

While this analysis is based on the concept of a well-isolated companion pion, that is, a 2+1 approximation, the capacity of the QMIPWA approach to absorb some three-body final-state interaction effects should be considered in the interpretation of the resulting (2-body) $\pi^-\pi^+$ S-wave amplitude obtained from the fit.

This is the first time that the $\pi^-\pi^+$ S-wave amplitude is extracted through a quasi-model-independent approach for the $D^+ \to \pi^-\pi^+\pi^+$ decay. The results provide an important input to phenomenological analyses, with the $\pi^+\pi^-$ scattering amplitude obtained continuously from threshold up to 1.7 GeV.

Table 4: Fitted magnitude and phase of the S-wave amplitude at each $\pi^-\pi^+$ mass knot, relative to the $\rho(770)^0\pi^+$ channel. The uncertainties quoted are, in order, statistical, experimental systematics and model systematics.

knot	$m_{\pi^-\pi^+}$ [GeV]	Magnitude	Phase [rad]
1	0.280	$15.2 \pm 0.3 \pm 1.5 \pm 0.5$	$1.67 \pm 0.03 \pm 0.06 \pm 0.02$
2	0.322	$15.9 \pm 0.3 \pm 0.9 \pm 0.4$	$1.55 \pm 0.02 \pm 0.06 \pm 0.02$
3	0.364	$15.5 \pm 0.2 \pm 0.6 \pm 0.4$	$1.65 \pm 0.02 \pm 0.04 \pm 0.02$
4	0.406	$16.1 \pm 0.2 \pm 0.9 \pm 0.4$	$1.79 \pm 0.02 \pm 0.05 \pm 0.02$
5	0.448	$14.8 \pm 0.2 \pm 0.5 \pm 0.3$	$1.89 \pm 0.02 \pm 0.10 \pm 0.02$
6	0.500	$15.8 \pm 0.2 \pm 2.7 \pm 0.3$	$2.18 \pm 0.02 \pm 0.11 \pm 0.02$
7	0.540	$13.4 \pm 0.2 \pm 0.7 \pm 0.3$	$2.18 \pm 0.02 \pm 0.05 \pm 0.02$
8	0.598	$11.8 \pm 0.2 \pm 0.5 \pm 0.3$	$2.33 \pm 0.02 \pm 0.06 \pm 0.02$
9	0.623	$10.7 \pm 0.2 \pm 0.3 \pm 0.2$	$2.35 \pm 0.02 \pm 0.04 \pm 0.02$
10	0.647	$10.1 \pm 0.2 \pm 0.4 \pm 0.2$	$2.39 \pm 0.02 \pm 0.06 \pm 0.02$
11	0.660	$9.8 \pm 0.2 \pm 0.4 \pm 0.2$	$2.47 \pm 0.02 \pm 0.04 \pm 0.02$
12	0.700	$8.4 \pm 0.2 \pm 0.5 \pm 0.2$	$2.49 \pm 0.02 \pm 0.05 \pm 0.02$
13	0.775	$7.7 \pm 0.1 \pm 0.6 \pm 0.1$	$2.60 \pm 0.02 \pm 0.09 \pm 0.01$
14	0.800	$6.3 \pm 0.2 \pm 0.6 \pm 0.1$	$2.71 \pm 0.03 \pm 0.08 \pm 0.02$
15	0.850	$3.4 \pm 0.1 \pm 0.5 \pm 0.1$	$2.55 \pm 0.06 \pm 0.21 \pm 0.03$
16	0.900	$2.3 \pm 0.1 \pm 0.3 \pm 0.1$	$1.88 \pm 0.08 \pm 0.10 \pm 0.05$
17	0.921	$3.5 \pm 0.1 \pm 0.3 \pm 0.1$	$1.23 \pm 0.05 \pm 0.25 \pm 0.03$
18	0.951	$6.5 \pm 0.1 \pm 0.3 \pm 0.1$	$1.37 \pm 0.04 \pm 0.04 \pm 0.02$
19	0.968	$11.4 \pm 0.2 \pm 1.0 \pm 0.1$	$1.35 \pm 0.03 \pm 0.48 \pm 0.01$
20	0.980	$15.7 \pm 0.2 \pm 3.0 \pm 0.1$	$2.31 \pm 0.04 \pm 0.92 \pm 0.01$
21	0.985	$12.8 \pm 0.2 \pm 1.2 \pm 0.1$	$2.40 \pm 0.05 \pm 0.91 \pm 0.01$
22	0.993	$9.0 \pm 0.1 \pm 2.6 \pm 0.0$	$2.40 \pm 0.04 \pm 0.27 \pm 0.01$
23	1.010	$8.4 \pm 0.1 \pm 0.8 \pm 0.1$	$2.27 \pm 0.03 \pm 0.27 \pm 0.01$
24	1.078	$6.8 \pm 0.1 \pm 0.1 \pm 0.1$	$2.60 \pm 0.03 \pm 0.07 \pm 0.02$
25	1.100	$5.1 \pm 0.1 \pm 0.3 \pm 0.1$	$2.75 \pm 0.04 \pm 0.08 \pm 0.02$
26	1.135	$3.8 \pm 0.1 \pm 0.2 \pm 0.1$	$2.38 \pm 0.05 \pm 0.07 \pm 0.03$
27	1.160	$3.5 \pm 0.1 \pm 0.1 \pm 0.1$	$2.08 \pm 0.05 \pm 0.08 \pm 0.03$
28	1.193	$3.5 \pm 0.1 \pm 0.1 \pm 0.1$	$1.84 \pm 0.05 \pm 0.07 \pm 0.03$
29	1.210	$3.6 \pm 0.1 \pm 0.1 \pm 0.1$	$1.75 \pm 0.05 \pm 0.08 \pm 0.03$
30	1.235	$3.5 \pm 0.1 \pm 0.2 \pm 0.1$	$1.68 \pm 0.04 \pm 0.12 \pm 0.04$
31	1.267	$3.5 \pm 0.1 \pm 0.3 \pm 0.1$	$1.59 \pm 0.04 \pm 0.13 \pm 0.04$
32	1.297	$3.6 \pm 0.1 \pm 0.3 \pm 0.2$	$1.53 \pm 0.04 \pm 0.15 \pm 0.04$
33	1.323	$3.5 \pm 0.1 \pm 0.4 \pm 0.2$	$1.46 \pm 0.04 \pm 0.16 \pm 0.05$
34	1.352	$3.6 \pm 0.1 \pm 0.4 \pm 0.2$	$1.26 \pm 0.04 \pm 0.14 \pm 0.05$
35	1.376	$3.3 \pm 0.1 \pm 0.5 \pm 0.2$	$1.13 \pm 0.04 \pm 0.18 \pm 0.07$
36	1.402	$3.9 \pm 0.2 \pm 0.5 \pm 0.2$	$0.93 \pm 0.04 \pm 0.10 \pm 0.06$
37	1.427	$5.6 \pm 0.2 \pm 0.4 \pm 0.2$	$0.88 \pm 0.03 \pm 0.10 \pm 0.05$
38	1.455	$8.0 \pm 0.2 \pm 0.3 \pm 0.2$	$1.09 \pm 0.02 \pm 0.08 \pm 0.04$
39	1.475	$8.9 \pm 0.2 \pm 0.5 \pm 0.2$	$1.27 \pm 0.02 \pm 0.10 \pm 0.04$
40	1.492	$9.4 \pm 0.2 \pm 0.9 \pm 0.3$	$1.59 \pm 0.02 \pm 0.07 \pm 0.03$
41	1.524	$6.7 \pm 0.2 \pm 0.3 \pm 0.4$	$2.04 \pm 0.03 \pm 0.30 \pm 0.04$
42	1.557	$4.5 \pm 0.2 \pm 0.7 \pm 0.3$	$1.78 \pm 0.05 \pm 0.18 \pm 0.08$
43	1.577	$5.2 \pm 0.2 \pm 0.4 \pm 0.3$	$1.58 \pm 0.05 \pm 0.10 \pm 0.08$
44	1.598	$6.0 \pm 0.2 \pm 0.4 \pm 0.3$	$1.67 \pm 0.05 \pm 0.27 \pm 0.07$
45	1.619	$5.6 \pm 0.2 \pm 0.8 \pm 0.4$	$1.80 \pm 0.06 \pm 0.24 \pm 0.07$
46	1.640	$6.6 \pm 0.2 \pm 0.3 \pm 0.4$	$1.86 \pm 0.05 \pm 0.14 \pm 0.06$
47	1.660	$5.6 \pm 0.3 \pm 0.5 \pm 0.4$	$1.81 \pm 0.06 \pm 0.15 \pm 0.08$
48	1.687	$5.4 \pm 0.3 \pm 1.7 \pm 0.5$	$1.93 \pm 0.08 \pm 0.60 \pm 0.10$
49	1.711	$1.8 \pm 0.4 \pm 2.5 \pm 0.6$	$2.57 \pm 0.37 \pm 2.33 \pm 0.34$
50	1.730	$8.2 \pm 0.8 \pm 8.0 \pm 0.7$	$-0.20 \pm 0.23 \pm 1.71 \pm 0.04$

References

[1] Particle Data Group, P. A. Zyla *et al.*, *Review of particle physics*, Prog. Theor. Exp. Phys. **2020** (2020) 083C01.

[2] N. N. Achasov *et al.*, *Evidence of the four-quark nature of $f_0(980)$ and $f_0(500)$*, Phys. Rev. **D103** (2021) 014010, `arXiv:2009.04191`.

[3] E. Klempt and A. Zaitsev, *Glueballs, hybrids, multiquarks. Experimental facts versus QCD inspired concepts*, Phys. Rept. **454** (2007) 1, `arXiv:0708.4016`.

[4] J. R. Peláez, *From controversy to precision on the sigma meson: a review on the status of the non-ordinary $f_0(500)$ resonance*, Physics Reports **658** (2016) 1.

[5] N. N. Achasov, *37 years with the light scalar mesons. The learned lessons*, Phys. Part. Nucl. **48** (2017) 681.

[6] W. Ochs, *The status of glueballs*, Journal of Physics G: Nuclear and Particle Physics **40** (2013) 043001.

[7] B. Hyams *et al.*, *$\pi\pi$ phase-shift analysis from 600 to 1900 MeV*, Nucl. Phys. **B64** (1973) 134.

[8] B. Hyams *et al.*, *A study of $\pi\pi$ phase shift solutions in the mass region 1.0 to 1.8 GeV from $\pi^-p \to \pi^-\pi^+n$ at 17.2 GeV*, Nucl. Phys. **B100** (1975) 205.

[9] S. D. Protopopescu *et al.*, *$\pi\pi$ partial wave analysis from reactions $\pi^+p \to \pi^+\pi^-\Delta^{++}$ and $\pi^+p \to K^+K^-\Delta^{++}$ at 7.1 GeV/c*, Phys. Rev. **D7** (1973) 1279.

[10] G. Grayer *et al.*, *High statistics study of the reaction $\pi^-p \to \pi^-\pi^+n$: Apparatus, method of analysis, and general features of results at 17 GeV/c*, Nucl. Phys. **B75** (1974) 189.

[11] CERN-Cracow-Munich collaboration, H. Becker *et al.*, *A model independent partial wave analysis of the $\pi^+\pi^-$ system produced at low four momentum transfer in the reaction π^-p (polarized) $\to \pi^+\pi^-n$ at 17.2- GeV/c*, Nucl. Phys. **B151** (1979) 46.

[12] L. Rosselet *et al.*, *Experimental study of 30,000 K_{e4} decays*, Phys. Rev. **D15** (1977) 574.

[13] BNL-E865 collaboration, S. Pislak *et al.*, *A new measurement of K_{e4}^+ decay and the s-wave $\pi\pi$ scattering length a_0^0*, Phys. Rev. Lett. **87** (2001) 221801, `arXiv:hep-ex/0106071`, [Erratum: Phys.Rev.Lett. 105, 019901 (2010)].

[14] I. Bediaga and C. Göbel, *Direct CP violation in beauty and charm hadron decays*, Prog. Part. Nucl. Phys. **114** (2020) 103808, `arXiv:2009.07037`.

[15] E791 collaboration, E. M. Aitala *et al.*, *Experimental evidence for a light and broad scalar resonance in $D^+ \to \pi^-\pi^+\pi^+$ decay*, Phys. Rev. Lett **86** (2001) 770.

[16] FOCUS collaboration, J. M. Link *et al.*, *Dalitz plot analysis of D_s^+ and D^+ decay to $\pi^+\pi^-\pi^+$ using the K-matrix formalism*, Phys. Lett. **B585** (2004) 200.

[17] CLEO collaboration, G. Bonvicini *et al.*, *Dalitz plot analisis of the $D^+ \to \pi^- \pi^+ \pi^+$ decay*, Phys. Rev. **D76** (2007) 012001.

[18] BaBar collaboration, B. Aubert *et al.*, *Dalitz Plot Analysis of $D_s^+ \to \pi^+ \pi^- \pi^+$*, Phys. Rev. **D79** (2009) 032003, arXiv:0808.0971.

[19] BESIII collaboration, M. Ablikim *et al.*, *Amplitude analysis of the $D_s^+ \to \pi^+ \pi^- \pi^+$ decay*, arXiv:2108.10050.

[20] LHCb collaboration, R. Aaij *et al.*, *Amplitude analysis of the $D_s^+ \to \pi^- \pi^+ \pi^+$ decay*, LHCb-PAPER-2022-030, in preparation.

[21] LHCb collaboration, A. A. Alves Jr. *et al.*, *The LHCb Detector at the LHC*, JINST **3** (2008) S08005.

[22] LHCb collaboration, R. Aaij *et al.*, *LHCb detector performance*, Int. J. Mod. Phys. **A30** (2015) 1530022, arXiv:1412.6352.

[23] R. Aaij *et al.*, *The LHCb trigger and its performance in 2011*, JINST **8** (2013) P04022, arXiv:1211.3055.

[24] T. Sjöstrand, S. Mrenna, and P. Skands, *A brief introduction to PYTHIA 8.1*, Comput. Phys. Commun. **178** (2008) 852, arXiv:0710.3820; T. Sjöstrand, S. Mrenna, and P. Skands, *PYTHIA 6.4 physics and manual*, JHEP **05** (2006) 026, arXiv:hep-ph/0603175.

[25] I. Belyaev *et al.*, *Handling of the generation of primary events in Gauss, the LHCb simulation framework*, J. Phys. Conf. Ser. **331** (2011) 032047.

[26] D. J. Lange, *The EvtGen particle decay simulation package*, Nucl. Instrum. Meth. **A462** (2001) 152.

[27] N. Davidson, T. Przedzinski, and Z. Was, *PHOTOS interface in C++: Technical and physics documentation*, Comp. Phys. Comm. **199** (2016) 86, arXiv:1011.0937.

[28] Geant4 collaboration, J. Allison *et al.*, *Geant4 developments and applications*, IEEE Trans. Nucl. Sci. **53** (2006) 270; Geant4 collaboration, S. Agostinelli *et al.*, *Geant4: A simulation toolkit*, Nucl. Instrum. Meth. **A506** (2003) 250.

[29] M. Clemencic *et al.*, *The LHCb simulation application, Gauss: Design, evolution and experience*, J. Phys. Conf. Ser. **331** (2011) 032023.

[30] D. Müller, M. Clemencic, G. Corti, and M. Gersabeck, *ReDecay: A novel approach to speed up the simulation at LHCb*, Eur. Phys. J. **C78** (2018) 1009, arXiv:1810.10362.

[31] A. Hoecker *et al.*, *TMVA 4 — Toolkit for multivariate data analysis with ROOT. Users guide.*, arXiv:physics/0703039.

[32] L. Breiman, J. Friedman, C. J. Stone, and R. A. Olshen, *Classification and regression trees*, CRC press, 1984.

[33] A. Rogozhnikov, *Reweighting with boosted decision trees*, in *Journal of Physics: Conference Series*, **762**, 012036, IOP Publishing, 2016.

[34] M. Pivk and F. R. Le Diberder, *sPlot: A statistical tool to unfold data distributions*, Nuclear Instruments and Methods in Physics Research Section A: Accelerators, Spectrometers, Detectors and Associated Equipment **555** (2005) 356 .

[35] T. Skwarnicki, *A study of the radiative cascade transitions between the Upsilon-prime and Upsilon resonances*, PhD thesis, Institute of Nuclear Physics, Krakow, 1986, DESY-F31-86-02.

[36] J. Back *et al.*, *Laura++: a Dalitz plot fitter*, Computer Physics Communications **231** (2018) 198.

[37] L. Anderlini *et al.*, *The PIDCalib package*, LHCb-PUB-2016-021, 2016.

[38] J. Blatt and J. Weisskopf, *Theoretical Nuclear Physics*, John Wiley and Sons, 1952.

[39] CLEO collaboration, G. Bonvicini *et al.*, *Dalitz plot analysis of the $D^+ \to K^-\pi^+\pi^+$ decay*, Phys. Rev. **D78** (2008) 052001.

[40] LHCb collaboration, R. Aaij *et al.*, *Dalitz plot analysis of the decay $D^+ \to K^-K^+K^+$*, JHEP **04** (2019) 063, arXiv:1902.05884.

[41] LHCb collaboration, R. Aaij *et al.*, *Observation of sizeable ω contribution to $\chi_{c1} \to \pi^+\pi^- J/\psi$ decays*, arXiv:2204.12597, submitted to PRL.

[42] C. Zemach, *Three-pion decays of unstable particles*, Phys. Rev. **B133** (1964) 1201.

[43] G. Gounaris and J. Sakurai, *Finite-width corrections to the vector-meson-dominance prediction for $\rho \to e^+e^-$*, Phys. Rev. Lett. **21** (1968) 244.

[44] P. E. Rensing, *Single electron detection for SLD CRID and multi-pion spectroscopy in K-p interactions at 11- GeV/c*, PhD thesis, SLAC, 1993.

[45] R. R. Akhmetshin *et al.*, *Measurement of $e^+e^- \to \pi^+\pi^-$ cross-section with CMD-2 around ρ-meson*, Phys. Lett. **527** (2002) 161.

[46] H. Schreiner *et al.*, *Goofit 2.0*, Journal of Physics: Conference Series **1085** (2017) .

[47] F. James, *MINUIT function minimization and error analysis: Reference manual version 94.1*, 1994. CERN-D506.

[48] M. Williams, *How good are your fits? Unbinned multivariate goodness-of-fit tests in high energy physics*, Journal of Instrumentation **5** (2010) P09004.

[49] CMD-2 collaboration, R. R. Akhmetshin *et al.*, *High-statistics measurement of the pion form factor in the ρ-meson energy range with the CMD-2 detector*, Phys. Lett. **B648** (2007) 28, arXiv:hep-ex/0610021.

[50] CDF collaboration, A. Abulencia *et al.*, *Measurement of the dipion dass dpectrum in $X(3872) \to J/\psi\pi^+\pi^-$ decays*, Phys. Rev. Lett. **96** (2006) 102002.

[51] Belle collaboration, S.-K. Choi *et al.*, *Bounds on the width, mass difference and other properties of $X(3872) \to \pi^+\pi^- J/\psi$ decays*, Phys. Rev. **D84** (2011) 052004.

[52] BESIII collaboration, M. Ablikim *et al.*, *Precision study of $\eta' \to \gamma\pi^+\pi^-$ decay dynamics*, Phys. Rev. Lett. **120** (2018) 242003, `arXiv:1712.01525`.

[53] LHCb collaboration, R. Aaij *et al.*, *Amplitude analysis of the $B^+ \to \pi^+\pi^+\pi^-$ decay*, Phys. Rev. **D101** (2020) 012006, `arXiv:1909.05211`.